

## **Section 5**

Development of and studies with regional and convective-scale atmospheric models and ensembles.



## **Operational Convective-Scale Numerical weather prediction model and high resolution city scale model at NCMRWF**

**A. Jayakumar, Saji Mohandas, T. J. Anurose, V. S. Prasad**

*National Centre for Medium Range Weather Forecast (NCMRWF), Ministry of Earth Sciences, India*

India recently witnessed severe weather episodes such as flash floods, thunderstorm, dust storm, pollution episodes etc under a warming climate. A reliable forecast for the variables associated to aforementioned dynamic tropical systems is one of the mandates of the NCMRWF. Subsequently, the seamless prediction system of Unified Model (UM) at a range of scales is employed for a step-change in the severe weather prediction.

**Convective-Scale model :** A convective scale model covering Indian domain with a gridded length of 4km is setup for generating 75hour forecast based on 00 UTC and 12 UTC initial conditions. The model employs NASA Shuttle Radar Topographic Mission (SRTM) 90m digital elevation map orography. It has a rotated latitude-longitude horizontal grid with Arakawa-C staggering and a terrain-following hybrid vertical coordinate with Charney-Philips staggering. The domain covers (62°E-106 °E; 6 °S 41 °N) with 1200x1200 grid points horizontally and 90 hybrid levels in the vertical with a top at 40km. Lateral boundary and initial conditions are downscaled from the operational NCMRWF Unified model at 12 km resolution.

The science configuration of this model is based on UK Met Office science version “Regional Atmosphere and Land version 3” (RAL3), operationalised from 1 October, 2022. The model explicitly represents deep convective processes within the resolved dynamics, and a comprehensive set of parameterization schemes from the earlier version includes a double moment cloud microphysics scheme (CASIM: Cloud-Aerosol Interactive Microphysics) and Bi-modal cloud generation scheme (BM) (Field et al., 2023). Five hydrometeor species such as cloud, liquid, rain, ice, snow and graupel are represented within a cloud by CASIM, while a sub-grid cloudiness and cloud water content are diagnosed by BM, allowing for two modes of variability in the entrainment zones. Other physical schemes used here follow the one defined in the earlier operational models at NCMRWF ( Jayakumar et al., 2021a).

Figure 1 is one of the example prepared during, ‘Mocha’, severe cyclonic storm of the decade, where the snap shot of the real time forecast (t+48hour) of total lightning flashes, wind gust maxima, Dust AOD, mean surface dust and winds made available as a severe weather warning for India Meteorology Department (IMD), and other users. Here lighting flash is diagnosed from blended electric scheme depends on ice hydrometeor distribution and the dust forecast is from a prognostic mineral dust six bin scheme.

**City-scale model :** The DM-Chem is the city scale modeling system for every winter seasons to provide fog and visibility predictions, and also targeting air quality forecast from this year onwards. Physics change details are of the latest configuration of the DM-Chem (based on the RAL3) from the first release of this model (Jayakumar et al., 2021b). The emissions are prescribed by EDGAAR inventory in the outer 1.5 km nest and high-resolution IITM SAFAR inventory for the inner 330 m domain. The 24-hr forecasts of the previous day from the 1.5 km and 330 m models are used to initialize the chemistry and aerosols at the start of each cycle, whereas other fields are initialized and laterally mixed similar to the setup of a limited area Convective-Scale model.

Prognostic aerosol number and mass from United Kingdom Chemistry and Aerosols (UKCA) are coupled to CASIM for predicting number concentration of cloud and ice. A detailed urban canopy parameterisation, the Met Office Reading Urban Surface Exchange Scheme (MORUSES) is developed based on the local urban morphology (Anurose et al., 2022). The Delhi urban morphology data is derived

in collaboration with Indian Institute of Remote Sensing (IIRS) and is used for generating the empirical relationships between the urban morphological parameters and urban land-use fraction. Diurnally varying anthropogenic heat flux (QF) is estimated in the MORUSES scheme using a top-down, energy-consumption inventory method, which was derived based on socio economic statistics and energy consumption data for Delhi. Flexible interactive dry deposition scheme, treating 6 chemical species, is introduced in the land surface model of DM-Chem. The scheme considered three ‘resistance’ analogies to calculate deposition velocity such as Aerodynamic resistance (depends on the surface types), boundary layer resistance (depends on the species diffusion coefficient) and canopy resistance. The real-time daily biomass emissions datasets are initiated using Global Fire Assimilation System (GFAS) with one-day delayed.

## References

Anurose, T. J., Jayakumar, A., Gupta, K., Mohandas, S., Hendry, M. A., Smith, D. K. E., Francis, T., Bhati, S., Parde, A. N., Mohan, M., Mitra, A. K., Gupta, P. K., Chauhan, P., Jenamani, R., & Ghude, S. (2022). Implementation of the urban parameterization scheme to the Delhi model with an improved urban morphology. *Quarterly Journal of the Royal Meteorological Society*. <https://doi.org/10.1002/qj.4382>

Jayakumar A., Mohandas, S., George, J.P., Duttta, D., Routray, A., Prasad, S.K., Sarkar, A., & Mitra, A.K. (2021a). NCMRWF Regional Model Version 4 (NCUM-R: V4), NCMRWF Technical Report, NMRWF/TR/03/2021, March 2021, 27pp.

Jayakumar, A., Gordon, H., Francis, T., Hill, A.A., Mohandas, S., Sandeepan, B.S., Mitra, A.K. and Beig, G. (2021b) Delhi Model with Chemistry and aerosol framework (DM-Chem) for high-resolution fog forecasting. *Quarterly Journal of the Royal Meteorological Society*, 147(741), 3957–3978, <https://doi.org/10.1002/qj.4163>

Field, P. R., Hill, A., Shipway, B., Furtado, K., Wilkinson, J., Miltenberger, A., Gordon, H., Grosvenor, D. P., Stevens, R., and Van Weverberg, K.: Implementation of a Double Moment Cloud Microphysics Scheme in the UK Met Office Regional Numerical Weather Prediction Model, *Q. J. Roy. Meteorol. Soc.*, <https://doi.org/10.1002/qj.4414>

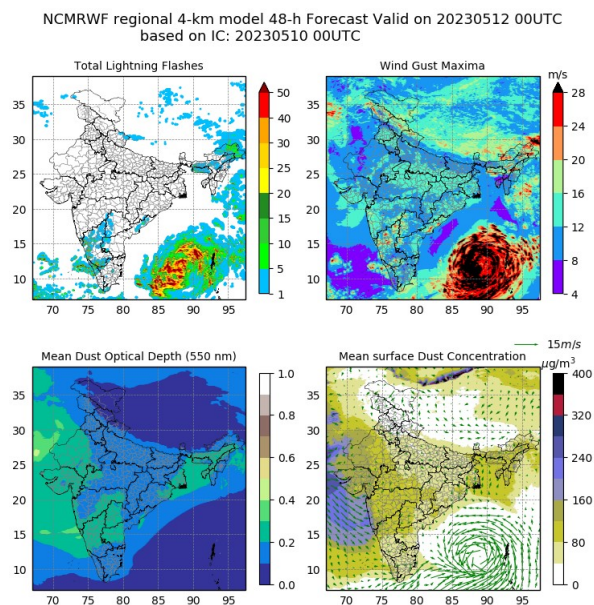


Figure 1. t+48 hour forecast from 4km model based on 20230510 00UTC initial condition.

# Scores of Initial Data for Limited-Area Modeling System COSMO-Ru from GME/ICON Global systems during 2012-2022 years: evaluation and peculiarities

D. Blinov<sup>1</sup>, A. Revokatova<sup>1,2</sup>, I. Rozinkina<sup>1</sup>, G. Rivin<sup>1,3</sup>

<sup>1</sup>Hydrometeorological Research Center of the Russian Federation, 13-1, Bolshoy Predtechensky lane, Moscow, 123376, Russia

<sup>2</sup>Yu. A. Izrael Institute of Global Climate and Ecology, Glebovskaya 20B, Moscow 107258, Russia

<sup>3</sup>Lomonosov Moscow State University, GSP-1, Leninskie Gory, Moscow 119991, Russia

\*Correspondence: denisblinov@ya.ru, revokatova@gmail.com; gdaly.rivin@mail.ru; inna.rozinkina@mail.ru

## Introduction

A limited-area numerical weather prediction (NWP) requires initial and boundary conditions, which often are prepared by interpolation of results of global weather forecasting systems. Hydrometeorological Center of Russia has been using the limited area NWP system COSMO-Ru since 2009 [1], for forecasting up to 5 days. The COSMO model [cosmo-model.org] is a core of the COSMO-Ru system. The results of global models of the German weather service (DWD) GME and ICON [2,3,4] have been used as initial and boundary conditions. During period 2012-2022 the global forecasting system of DWD was cardinally upgraded: at 2015 model ICON replaced GME in operational runs, subsequently some improvements in ICON model and in conjugate Data Assimilation system (DAS) have been introduced.

The authors of this paper analyzed errors of the COSMO-Ru zero lead time forecasts for the period 2012-2022 w.r.t. measurements from synoptic and aerologic stations on the territory of Russia. The variability of scores in dependence on regions and on different criteria as seasons, day times, and orography was analyzed and some typical features were detected.

The results of this study are important to understand the quality of initial data for limited-area modelling provided by the DWD global modelling system and to estimate possible effects of further implementation of the regional data assimilation in COSMO-Ru which is currently under development at the Hydrometcenter of Russia.

## Methodology

The results of DWD global modeling systems (DGM, mesh size is 13.2 km), for zero lead time (in fact – the product of included into DGM global Data assimilation system (DAS)) were transformed by COSMO-Ru system to the analyzed parameters at pre-specified vertical levels and in grid-boxes of COSMO-Ru13ENA configuration of COSMO model. The results were interpolated to the measurement points. The values of temperature and dew point at 2m height, wind velocity (module, direction, gusts) at 10m, pressure reduced to the sea level, cloudiness, parameters on standard geopotential surfaces from 1000 to 50 hPa were analyzed. The COSMO-Ru13ENA has the same horizontal mesh size as DGM products, but the coordinates of boxes are different. Using the archive of COSMO-Ru13ENA forecasts (available since 2012) we analyzed the time evolution of the quality of initial data as well as minimized the uncertainty

in the results associated with the use of different grid sizes.

The “forecast – observations” pairs were obtained using the nearest neighbor method. We examined the data for two seasons: Winter (DJF) and Summer (JJA) for the European territory of Russia (ETR) and its parts: Central Federal District (Central part of ETR) and South Federal District (North Caucasia). Some data for Siberia and Far East where also assessed. The analysis showed that the errors are generally larger in Siberia and the Far East in comparison with ETR. In this paper we provide the results for ETR only.

## Results

**1 Near-surface weather parameters.** The measured by meteorological network weather parameters are not used as initial data for model runs. They are not modeled directly but produced in a diagnostic manner. Nevertheless, these values at zero lead time can reflect a quality of initial data, taking into account some uncertainties related to the impact of the limited-area model producing them. Thus, the fields (first, the mean sea level pressure and wind at 10 m) obtained for mountain regions (e.g., Caucasia) with using the model relief showed the largest differences with observations.

Analyzing the scores for *Temperature and Dew Point at 2m height over land surface (T2m, TD2m)* we note large RMSE values for the data from 00:00 UTC runs and smaller values for 12:00 UTC in both seasons. The effect is most pronounced in summer. (Probably, this can be related to some problems in parametrizations under stable conditions as 00:00 UTC corresponds to night for ETR). Additionally, it's worth to note the evident improvement in modeling thermal conditions at the soil surface and the bottom model levels since 2014 that affect the quality of T2m (Fig. 1).

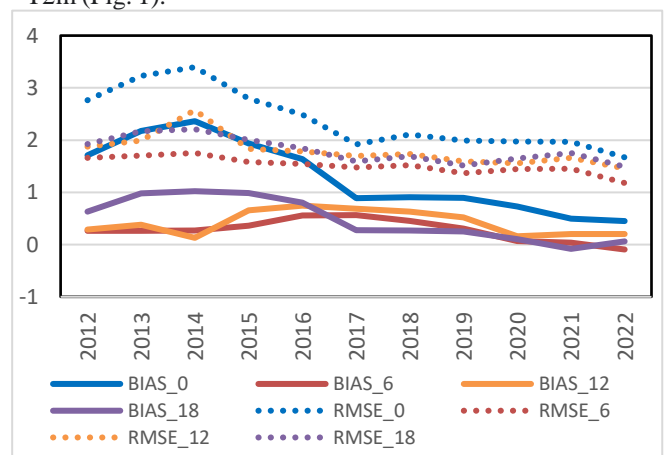


Fig. 1. T2m values for Summer: RMSE (dotted line) and BIAS (solid line). The UTC time of initial data is shown by colors.

The *Cloudiness* at zero lead time is mostly overestimated with its average error varying from 10 to 20%. However, for the data from 12:00 UTC (the warmest day time in European Russia), an efficient gradual improvement took place since 2015. For start fields of *Pressure reduced to Sea level (PMSL)* we can't see important trends of RMSE during the last 10 years. The BIAS changed from negative (2012, 2013) to positive (since 2014). The quality of initial data at 00:00 UTC often seems to be “the worst”, while the data at 06:00 and 18:00 UTC was the best (Fig. 2).

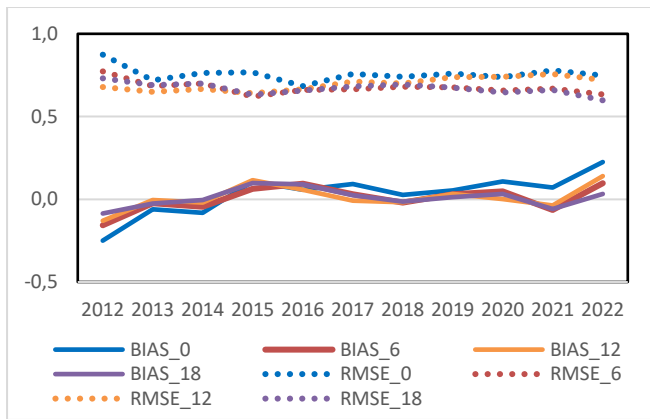


Fig. 2. PMSL values for Winter: RMSE (dotted line) and BIAS (solid line). The UTC time of initial data is shown by colors.

No clear conclusion could be made about the trends detected during the analyzed period. For 00:00 and 18:00 UTC the BIAS and RMSE decreased. **The maximum V10m values within a radius of 30 km around the measurement points** at 18:00 UTC in the summer have a noticeably larger RMSE than the ones from 00:00, 06:00 and 12:00. Besides, BIAS at 18:00 UTS is negative (**maximum V10m values underestimated**), while BIAS at 00, 12, 18 UTS tend to be positive after 2017 year. The winter data got worse since 2015, and the quality of the data for all initial times seem to be close to each other.

2. The errors of **free atmosphere fields** (interpolated to standard geopotential surface levels) do not demonstrate so strong dependence on daytime as most part of near-surface weather parameters (excluding the 1000 hPa level with the largest error). A comparison with radiosonde data reflects the quality of the initial data for modeling more objectively. The common features for the vertical profiles of the mean absolute error (MAE) for **temperature** are as follows: the maximum near the earth surface, a sharp decrease in the 1000-925 hPa layer, a gradual decrease in the 925-400 hPa layer, and a subsequent increase at the upper levels (as example, Fig.3). The MAE values at 1000 hPa are 1-1.1°C. The vertical profiles of error in the dew point temperature differ significantly from the temperature errors only at lower levels - there is no pronounced decrease in MAE from 1000 to 925 hPa. The MAE values from 1.2 to 2.4°C are maintained from the lower level up to 300 hPa, then it starts to grow. The analysis of temperature fields showed small changes in the free atmosphere errors from year to year for most layers and a decrease in large errors in upper-atmosphere fields after 2017 (Fig.3). Analysis of errors of **geopotential heights** showed a trend for their reduction over the analyzed period, more evident for layers up to 200 hPa. (Fig.3). **The assessment of vertical profiles of wind speed errors showed that** the interannual values are quite close, with errors in the range of 1.5–2 m/s up to a height of 100 hPa. A significant increase in errors is observed above 100 hPa in some years.

### Summary

The errors of zero lead time COSMO-Ru13ENA forecasts (being inherently the transformed initial data from GME/ICON Global systems during 2012-2022), demonstrate different behavior depending on dominant physical processes forming specific meteorological fields. The main features are as follows.

- A daily amplitude of errors of fields of near –

*surface parameters*: For the European part of Russia the 00:00 UTC runs (night time) demonstrate the maximal errors of *T2m* and *TD2m*, the greatest in winter, while the errors of *Psea* and *V10m* have maxima for 12:00 UTC runs, more pronounced in summer. Despite the fact that the above-listed fields are not directly taken from the initial data, the factors that caused the peculiarities of their errors can lead to differences between forecasts with long lead times (24 h or longer) started from initial data for different UTC times and valid at the same moment as well as to seasonal variations of forecast skill.

- *Seasonal variations*: In winter, larger errors demonstrate temperature, geopotential, and wind speed fields; in summer, wind direction, total cloudiness, and sea level pressure.

- *Variations in the vertical*: The biggest errors in all analyzed parameters (except for the V10m module) were found at bottom levels (up to 925 hPa) and at levels above 100 hPa.

- *An improvement of data quality* during the whole period (2012-2022) for the most part of the analyzed meteorological parameters. The step-like inter-year changes reflect the development of DWD global technology of Data assimilation and modelling, first – the transition from GME to ICON forecasting systems in 2015 and its further improvement.

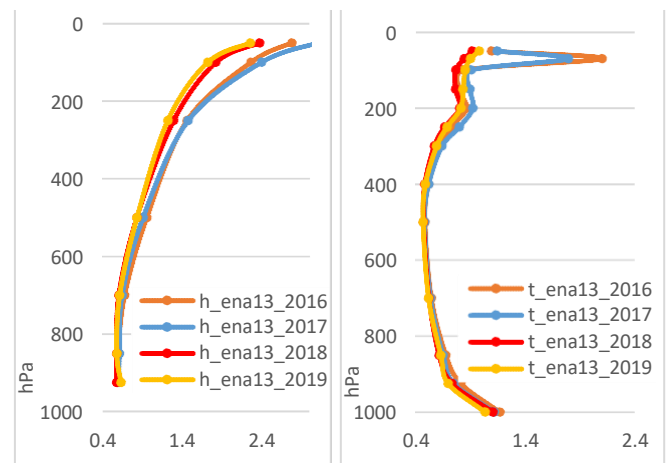


Fig 3. MAE of Geopotential (left) and Temperature (right) (Winter)

### References

1. Rivin G. S., Rozinkina I. A., Astakhova E. D. et al. COSMO-Ru high- resolution short-term numerical forecasting system, its development and applications // Hydrometeorological research and forecasts. - 2019. - No. 4 (374). - pp. 37-53.
2. Majewski D., Liermann D., Prohl P., Ritter B., Buchhold M., Hanisch T., Paul G., Wergen W., 2002: The operational global icosahedral- hexagonal grid point model GME: Description and high-resolution tests. Mon. Wea. Rev. – 2002. – 130. – P.319–338.
3. Zängl, G., D. Reinert, P. Ripodas, and M. Baldauf. The ICON (ICOsahedral Non-hydrostatic) modelling framework of DWD and MPI-M: Description of the non-hydrostatic dynamical core. // Q. J. R. Meteorol. Soc. – 2015. №141. – P. 563–579.
4. Schraff, C., H. Reich, A. Rhodin, A. Schomburg, K. Stephan, A. Perianez, and R. Potthast, 2016: Kilometre-scale ensemble data assimilation for the COSMO model (KENDA). Q.J.R. Meteorol. Soc., 142, 1453–1472.

# On the Development of NOAA's Rapid Refresh Forecast System

Jacob R. Carley<sup>1</sup>, Matthew E. Pyle<sup>1</sup>, Curtis R. Alexander<sup>2</sup>, and Stephen Weygandt<sup>2</sup>

<sup>1</sup>NOAA/NWS/NCEP/EMC, College Park, Maryland, USA

<sup>2</sup>NOAA/OAR/GSL, Boulder, CO, USA

Email: jacob.carley@noaa.gov

## 1. The Rapid Refresh Forecast System (RRFS)

This report describes the ongoing development of the RRFS, which is an hourly-updated, ensemble data assimilation and prediction system run at 3 km grid spacing covering North America. The RRFS is based on the Unified Forecast System (UFS) and is part of a larger effort to unify several operational National Weather Service regional, high-resolution modeling systems around a single UFS-based system.

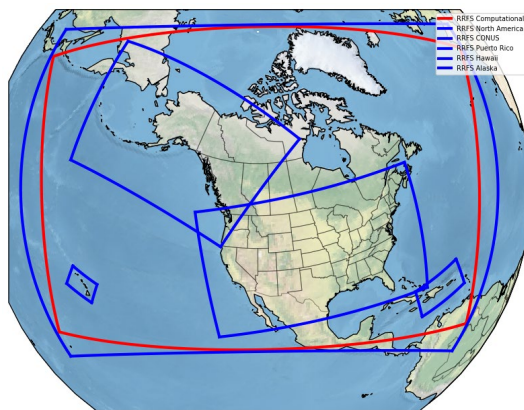


Fig. 1: Depiction of the prototype RRFS integration domain (in red) and output regions for gridded output (in blue)

## 2. Dynamics and Physics

The RRFS is based upon the fully compressible, nonhydrostatic Finite Volume Cubed-Sphere (FV3) dynamical core (Lin 2004; Harris et al. 2021) and uses the limited area model capability (Black et al. 2021). The gnomonic grid used for global applications has been replaced with an Extended Schmidt Gnomonic grid (Purser et al. 2020), which provides much more uniform grid spacing over a large regional domain than a purely gnomonic grid. The RRFS features 65 vertical layers with a 2 hPa model top. The vertical layers and model top were chosen based on a balance of forecast performance, computational expense, and a desire to improve the assimilation of satellite radiance observations with high peaking channels. The RRFS physical package is based upon the operational High Resolution Rapid Refresh (HRRR; Dowell et al. 2022) - which is planned to be subsumed upon the operational implementation of RRFS.

## 3. Data Assimilation

The RRFS data assimilation system (RDAS) is based upon a hybrid 3DEnVar-EnKF system. The EnKF, which features ~30 members, serves two purposes: (1) providing flow-dependent forecast error covariances in the hybrid 3DEnVar and (2) it provides the source for initial conditions for the ensemble free forecasts. The RDAS leverages a partial-cycling approach for the deterministic hybrid 3DEnVar analysis by way of a twice-a-day spin-up cycle that runs in parallel to the on-time analysis. At these times the atmospheric state in the RRFS is fully replaced with the atmospheric state from the corresponding best available forecast from the global model. At the same time, the 3 km land states are still preserved in the RDAS. This mitigates growing bias over a long period of cycling owing to a regional model's fundamental inability to resolve long wavelengths due to domain size. The RDAS assimilates a wide array of observations, which includes but is not limited to radar reflectivity and velocity, GOES ABI radiances, aircraft, rawinsonde, and surface observations. Land and soil states are updated via a simple covariance model with a one-coupling between the near-surface analysis increment and the underlying land state. The RDAS is designed such that analysis states are available at approximately  $t+40$ mins, where  $t$  is the cycle time (e.g., 1200 UTC).

## 4. Deterministic and Ensemble Forecasts

Forecasts from RRFS will include both a deterministic control running at an hourly cadence, and an ensemble system that produces forecasts every six hours. Both the deterministic and ensemble components will generate forecasts to 60 h for the 00/06/12/18 UTC synoptic cycles, and the deterministic alone will run to 18 h for the other cycles. The forecast ensemble will consist of five members; these will be combined with ensemble forecasts from the previous cycle and the two most recent deterministic runs to generate ensemble products from a total of ~12 members. The exact usage of time-lagged members, and whether it will be a single physics configuration matching the deterministic control, or a multi-physics configuration, remains to be decided. In either physics configuration, the forecast ensemble is planned to utilize stochastic physics perturbations to enhance forecast spread.

## 5. Preliminary Results and Concluding Remarks

Forecast verification statistics will be generated and compared against operational deterministic and ensemble baseline systems. Currently, most direct comparisons have been done with the operational HRRR system where the RRFS is proving to be competitive (Fig. 2).

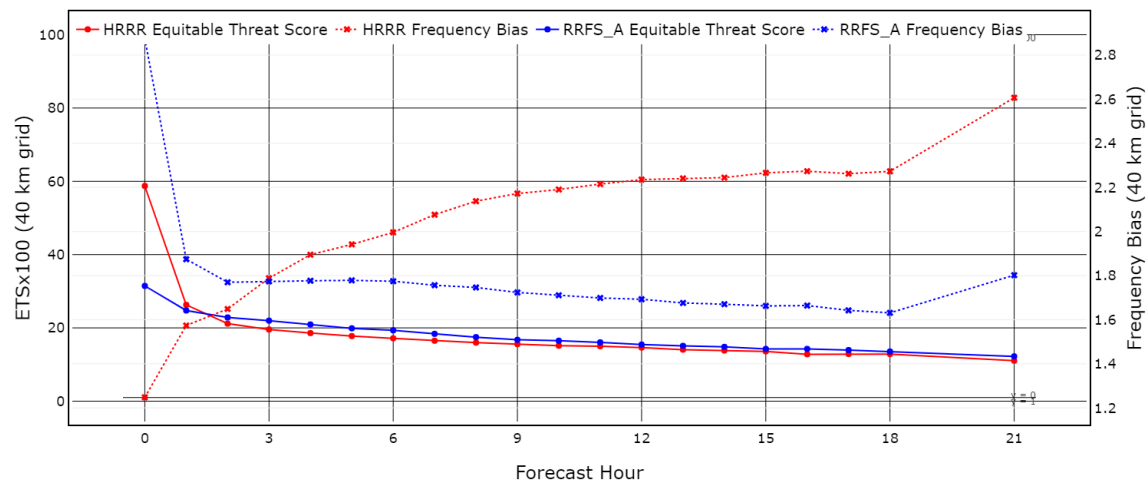


Fig. 2: Equitable Threat Score (solid) and Frequency Bias (dotted) for simulated composite reflectivity at the 30 dBZ threshold between March 20 and April 19, 2023, with forecast hour increasing along the abscissa, for the operational HRRR (red) and an RRFS prototype (blue). Verification scores were conducted on a common, upscaled 40-km grid.

The first version of the RRFS is expected to be finalized around Fall 2024. Remaining scientific priorities focus on addressing early feedback received from forecaster evaluations of prototype configurations, optimizing codes for speed and efficiency, finalizing the forecast ensemble, and tuning the data assimilation system.

## References

- Black, T. L., and Coauthors, 2021: A Limited Area Modeling Capability for the Finite-Volume Cubed-Sphere (FV3) Dynamical Core and Comparison With a Global Two-Way Nest. *Journal of Advances in Modeling Earth Systems*, 13, e2021MS002483, <https://doi.org/10.1029/2021ms002483>.
- Dowell, D. C., and Coauthors, 2022: The High-Resolution Rapid Refresh (HRRR): An hourly updating convection-allowing forecast model. Part I: Motivation and system description. *Wea. Forecasting*, 37, 1371-1395, <https://doi.org/10.1175/WAF-D-21-0151.1>
- Harris, L., X. Chen, L. Zhou, and J.-H. Chen, 2020: The Nonhydrostatic Solver of the GFDL Finite-Volume Cubed-Sphere Dynamical Core. NOAA Technical Memorandum OAR GFDL, 2020-003, <https://doi.org/https://doi.org/10.25923/9wdt-4895>.
- Lin, S.-J., 2004: A “Vertically Lagrangian” Finite-Volume Dynamical Core for Global Models. *Monthly Weather Review*, 132, 2293-2307, [https://doi.org/10.1175/1520-0493\(2004\)132%3C2293:AVLFDC%3E2.0.CO;2](https://doi.org/10.1175/1520-0493(2004)132%3C2293:AVLFDC%3E2.0.CO;2)
- Purser, R.J, D. Jovic, G. Ketefian, T. Black, J. Beck, J. Dong, and J. Carley, 2020: The extended Schmidt Gnomonic grid for regional applications. *1st UFS Users' Workshop*, July 27-29, 2020.

# Numerical simulations of a warm rain event observed in Tokyo, Japan

Akihiro Hashimoto<sup>1</sup> and Ryohei Misumi<sup>2</sup>

<sup>1)</sup> Meteorological Research Institute, Japan Meteorological Agency, Tsukuba, Japan

<sup>2)</sup> Department of Earth & Environmental Sciences, College of Humanities and Sciences, Nihon University, Tokyo, Japan

## 1. Introduction

Since 2016, continuous observations of clouds and aerosols have been performed at Tokyo Skytree which is the tallest broadcasting tower in the world, and the upper parts of the tower are often covered by low-level clouds (Misumi et al., 2018; 2022). Cloud droplets and aerosol particles were monitored at the 458 m level of Tokyo Skytree (35.71°N, 139.81°E, 460 m above sea level) to elucidate the cloud and precipitation processes in the Tokyo metropolitan area.

In the early morning of 22 July 2019, a warm rain precipitation system brought weak rainfall over Tokyo Skytree. This event is addressed to figure out its cloud and precipitation processes with numerical simulations. As the first step, we are investigating the dependency of simulation results on a choice of parameter values in modeled microphysics. This report gives the preliminary results of the sensitivity test to the parameters in the function giving the number concentration of cloud condensation nuclei.

## 2. Numerical simulations

A numerical simulation system was established based on the Japan Meteorological Agency's nonhydrostatic model (JMA-NHM, Saito et al., 2006). We first performed a simulation at a horizontal resolution of 5 km (5km-NHM) over a 2500 km × 2500 km wide domain as shown in Fig. 1a. Following this, a simulation with a 1 km horizontal resolution was performed (1km-NHM).

Corresponding author: Akihiro Hashimoto, Meteorological Research Institute, 1-1 Nagamine, Tsukuba, 305-0052, Japan. E-mail: ahashimo@mri-jma.go.jp

Table 1. The values of parameters that were given in the sensitivity test.

	$\alpha_x$	$\nu_x$	$C$	$k$
Exp I	3	1	300 cm <sup>-3</sup>	0.63
Exp II	3	1	3000 cm <sup>-3</sup>	0.63

In the 5km-NHM simulation, the top height of the model domain was 22.1 km. The vertical grid spacing ranged from 40 m at the surface to 723 m at the top of the domain. Sixty vertical layers in a terrain-following coordinate system were employed. The integration time was 45 hours, with a time-step of 15 s. The initial and boundary conditions were obtained from the JMA's mesoscale analysis data (MANAL). The initial time was set to 0300 JST (UTC+9) on 21 July 2019. Boundary conditions were provided every 3 hours.

The vertical grid arrangement in the 1km-NHM was the same as in the 5km-NHM, and the domain size was 500 km × 500 km (Fig. 1a). The integration time used was 30 hours with a timestep of 4 s. The initial and boundary conditions were obtained from the 5km-NHM simulation. The initial time for the 1km-NHM simulation was 6 hours later than that of the 5km-NHM.

In the 5km-NHM, we used the semi-double-moment bulk cloud microphysics scheme in which the mixing ratio and number concentration are predicted for solid hydrometeor classes (i.e., cloud ice, snow, and graupel), but only the mixing ratio is predicted for liquid hydrometeor classes (i.e., cloud water and rain). In the 1km-NHM, we used the option of a double-moment bulk cloud microphysics scheme to predict both the mixing ratio and number concentration of particles for all the hydrometeor

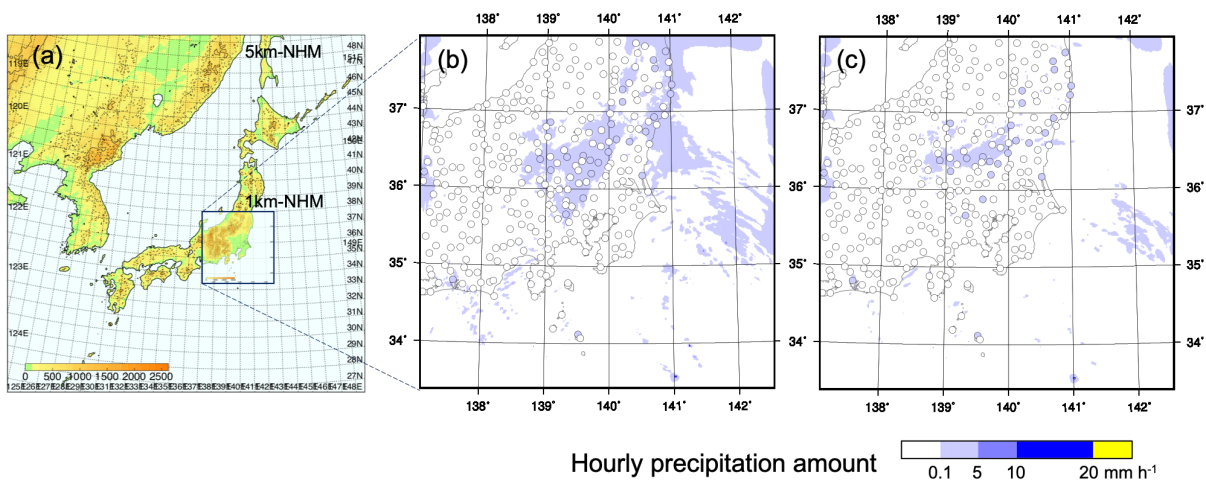


Fig. 1. (a) Computational domains for the numerical simulations: 5km- and 1km-NHM. (b) Hourly precipitation amount at 0300 JST on 22 July 2019 for Exp I. (c) Same as (b) but for Exp II. Circles show the observation stations of AMeDAS.

classes. Equation (1) shows the size spectra of liquid hydrometers (Cohard and Pinty, 2000).

$$n_x(D_x) = N_x \frac{\alpha_x}{\Gamma(\nu_x)} \lambda_x^{\alpha_x \nu_x} D_x^{\alpha_x \nu_x - 1} \exp[-(\lambda_x D_x)^{\alpha_x}], \quad (1)$$

where  $D_x$  is the diameter of a particle. Intercept parameter  $N_x$  and slope parameter  $\lambda_x$  are diagnosed every timestep using mixing ratio and number concentration of particles. Constant parameters  $\alpha_x$  and  $\nu_x$  are prescribed as 3.0 and 1.0, respectively. The index  $x = c$  and  $r$  indicate a parameter for cloud water and rain, respectively. The number concentration of cloud condensation nuclei (CCN) is given by the following function,

$$N_{CCN} = C S^k, \quad (2)$$

where  $S$  is the supersaturation ratio.  $C$  and  $k$  are constant parameters. We performed a sensitivity test Exp I and II by setting the  $(C, k)$  as  $(300 \text{ cm}^{-3}, 0.63)$  and  $(3000 \text{ cm}^{-3}, 0.63)$ , respectively (Table 1).

### 3. Results

Figures 1b and 1c show the hourly precipitation amount at 0300 JST on 21 July 2019 for Exp I and II, respectively. Circles show observation stations of the Automated Meteorological Data Acquisition System (AMeDAS). Precipitation in Exp I covered a larger area than in Exp II. Compared with the AMeDAS observation, the precipitation area was over- and underpredicted in Exp I and II, respectively, precipitation area. Figure 2 shows the vertically integrated mixing ratio of liquid and solid hydrometeors in the atmosphere (Liquid water dominated the total amount). Exp I (Fig. 1a) predicted less amount of hydrometeors than Exp II (Fig. 1b). Results shown in Figs 1b, 1c, and Fig. 2 indicate that more amount of water precipitated on the ground, thus less amount of water remained in the atmosphere in Exp I.

At Tokyo Skytree, cloud droplet number concentrations ( $N_c$ ) of  $50 - 100 \text{ cm}^{-3}$  were observed around 0300 JST on 21 July 2019. On the other hand, the predicted  $N_c$  ranged between  $40 - 80 \text{ cm}^{-3}$  during the same period in Exp I, while, in Exp II, the predicted  $N_c$  ranged between  $50 - 300 \text{ cm}^{-3}$  (not shown). The parameter values given in Exp I (Table 1) showed better results in the addressed precipitation event. Intermediate values between those used in Exp I and II probably are optimal. As it may not always be optimal to adopt the same values, we plan to extend the sensitivity test to other warm rain events observed at Tokyo Skytree.

#### Acknowledgment

This work was partly supported by the JSPS KAKENHI Grant Number 21H01163.

#### References

- Cohard, J. M., and J. P. Pinty, 2000: A comprehensive two-moment warm microphysical bulk scheme. Part I: Description and tests. *Quart. J. Roy. Meteor. Soc.*, **126**, 1815–1842.
- Misumi, R., Y. Uji, T. Tobo, K. Miura, J. Uetake, Y. Iwamoto, T.

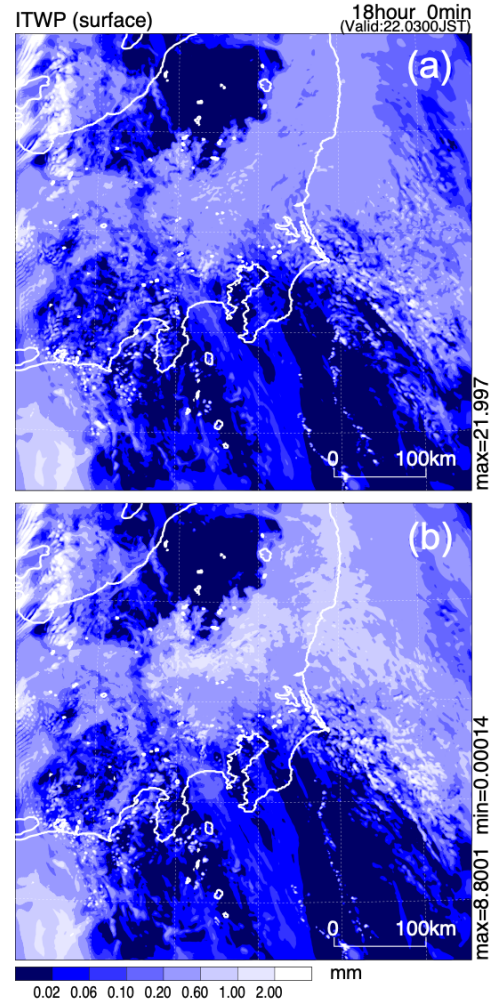


Fig. 2. Simulated distribution of vertically integrated mixing ratio of liquid and solid hydrometeors (mm) at 0300 JST on 22 July 2019 in (a) Exp I and (b) Exp II.

- Maesaka, and K. Iwanami, 2018: Characteristics of droplet size distributions in low-level stratiform clouds observed from Tokyo Skytree. *J. Meteor. Soc. Japan*, **96**, 405–413, doi:10.2151/jmsj.2018-040.
- Misumi, R., Y. Uji, K. Miura, T. Mori, Y. Tobo, Y. Iwamoto, 2022: Classification of aerosol-cloud interaction regimes over Tokyo. *Atmos. Res.*, **272**, 106150, doi:10.1016/j.atmosres.2022.106150.
- Saito, K., T. Fujita, Y. Yamada, J. Ishida, Y. Kumagai, K. Aranami, S. Ohmori, R. Nagasawa, S. Kumagai, C. Muroi, T. Kato, H. Eito, and Y. Yamazaki, 2006: The operational JMA nonhydrostatic mesoscale model. *Mon. Wea. Rev.*, **134**, 1266–1298.

# Implementation of the SPPT scheme in JMA's Mesoscale Ensemble Prediction System

\*KAWADA Hideyuki, KAKEHATA Takayuki, KAWANO Kohei  
Japan Meteorological Agency, Japan  
(Email: h.kawada@met.kishou.go.jp)

## 1. Introduction

JMA's Mesoscale Ensemble Prediction System (MEPS; Ono et al. 2021) has provided uncertainty information for the Agency's Meso-Scale Model since June 2019. In the system, perturbed members are produced using initial and lateral boundary perturbations, for which the production method was upgraded in September 2020 (Kakehata et al. 2021). Model uncertainties are not considered in the system.

Against such a background, the Stochastically Perturbed Parametrization Tendencies scheme (SPPT; Buizza et al. 1999, Palmer et al. 2009) was introduced into MEPS in March 2023 to account for model uncertainties. This report outlines the implementation and related effects.

## 2. SPPT scheme

SPPT is intended to represent the uncertainty of physical processes based on perturbation of related tendencies. The perturbed tendency of the physical process,  $X_p$ , is

$$X_p = (1 + r_X)X_c,$$

where  $r_X$  is a Gaussian random number correlated in space-time and  $X_c$  is the physical process tendency. The random number amplitude was set as 0.5, the correlation time as 6 hours, and the spatial correlation length as 500 km, and these parameters were tuned in preliminary experiments. For computational stability, only convection and radiation scheme tendencies were perturbed.

## 3. Initial perturbation adjustment

With the introduction of SPPT, the amplitude of the initial perturbation was readjusted. The previous MEPS ensemble spread (Figure 1, left)

tended to be over-dispersive in relation to the ensemble mean RMSE (Figure 1, right), especially in the JPN area (25 – 45°N, 125 – 145°E). To optimize the spread-skill relationship, the amplitude of the initial perturbation was set to 95% of the related value in the previous MEPS.

## 4. Verification results

To verify the effects of these changes, comparative experiments were conducted using the previous (CNTL) and upgraded (TEST) versions for July 1 – 31 2020 and January 20 – February 25 2020.

The spatial distribution of the TEST spread decreased in the JPN area and increased near the lateral boundary (Figure 2, left) due to the dominant influence of initial perturbation in the JPN area, while the effect of SPPT extends to the entire forecast area. TEST results showed mitigation of the undesirable characteristics of over-dispersiveness in CNTL spread for the JPN area and under-dispersiveness near the lateral boundary as compared to the RMSE of the ensemble mean (Figure 2, right). The same results were obtained in the winter experiment (not shown). The time series of the spread-skill relationship (Figure 3) shows that over-dispersion up to the 15-hour forecast for the JPN area (left) and under-dispersion after the 12-hour forecast for the entire forecast area (right) were both reduced.

For precipitation probability forecasts, the Brier-Skill Score (BSS) shows improvement for the summer experiment at each threshold value (Figure 4, left). In the winter experiment, BSS is nearly neutral for thresholds at which it is more skillful than the climatological forecast (Figure 4,

right). TEST precipitation distributions for each member were often not significantly different from those of CNTL (not shown). However, in some cases, TEST exhibited a higher probability of heavy rain where the convection scheme was activated (not shown). This may contribute to the improved probability seen in precipitation forecasts.

## 5. Summary

The results of the research showed that introduction of SPPT into MEPS and adjustment of the amplitude of initial perturbations improved ensemble spread and precipitation probability forecasts. JMA's operational system was updated accordingly in March 2023.

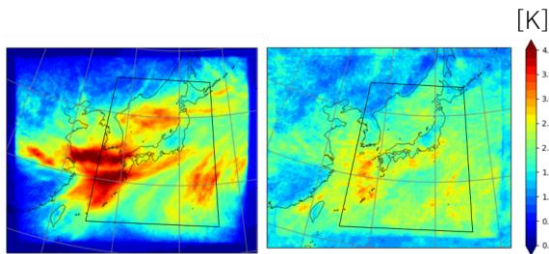


Figure 1. One-month (July 2020) average of ensemble spread (left) and RMSE of ensemble mean (right) for 850 hPa equivalent potential temperature (K) at T+9 for the previous MEPS (CNTL). Black frame: JPN area.

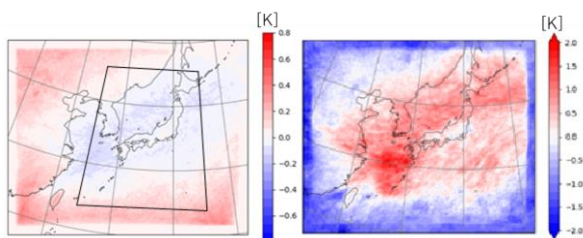


Figure 2. Spread difference between CNTL and TEST (left); difference between CNTL spread and RMSE of the ensemble mean of CNTL (right), both for 850 hPa equivalent potential temperature (K) at T+9 for the summer experiment. Right: differences between left and right in Figure 1.

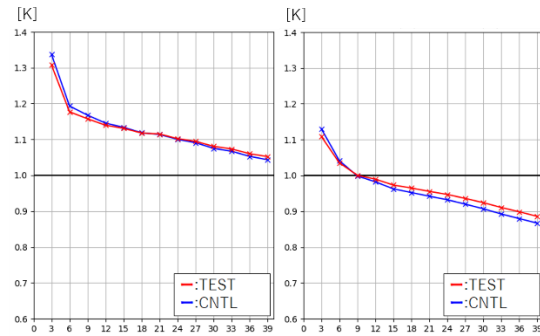


Figure 3. Time series (39 hours) of spread-skill relationship in the JPN area (left) and the entire forecast area (right) of 850 hPa equivalent potential temperature (K) for the summer experiment. Values are defined by the ratio of spread to RMSE, and are considered over-dispersive above 1 and under-dispersive below 1. The horizontal axis is the forecast range (hours).

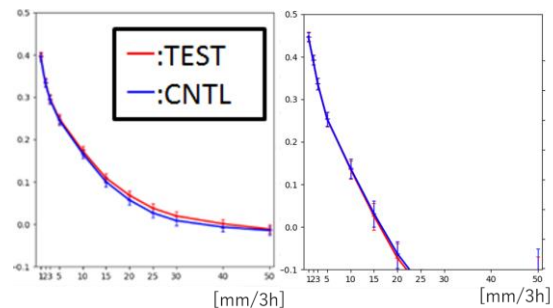


Figure 4. BSS of 3-hour cumulative precipitation probabilistic forecasting in CNTL (blue) and TEST (red) for the summer (left) and winter (right) experiments. Horizontal axis: threshold.

## References

- Buizza, R., M. Miller, and T. N. Palmer, 1999: Stochastic representation of model uncertainties in the ECMWF ensemble prediction system. *Quart. J. Roy. Meteor. Soc.*, 125, 2887-2908.
- Kakehata, K., M. Kunii, K. Kawano, and H. Kawada, 2021: Upgrades of JMA's Mesoscale Ensemble Prediction System. *CAS/JSC WGNE Res. Activ. Earth System Modell.*, 51, 5.05–5.06.
- Ono, K., M. Kunii, and Y. Honda, 2021: The regional model-based Mesoscale Ensemble Prediction System, MEPS, at the Japan Meteorological Agency. *Quart. J. Roy. Meteor. Soc.*, 147, 465–484.
- Palmer, T. N., R. Buizza, F. Doblas-Reyes, T. Jung, M. Leutbecher, G. J. Shutts, M. Steinheimer, and A. Weisheimer, 2009: Stochastic parametrization and model uncertainty. *ECMWF Tech. Memo*, 598, 42 pp.

# Assessment of the impact of a modified sea ice edge on the forecast and development of polar lows: simulation of the case-study using the ICON model

Anastasia Revokatova<sup>1,2,\*</sup>, Mikhail Nikitin<sup>1</sup>, Gdaliy Rivin<sup>1,3,\*</sup>, Inna Rozinkina<sup>1,\*</sup>, Denis Blinov<sup>1</sup> and Ekaterina Tatarinovich<sup>1</sup>

<sup>1</sup> Hydrometeorological Research Center of the Russian Federation, Bolshoi Predtechensky per. 13-1, Moscow 123242, Russia;

<sup>2</sup> Yu. A. Izrael Institute of Global Climate and Ecology, Glebovskaya 20B, Moscow 107258, Russia

<sup>3</sup> Geographic Faculty, Department of Meteorology and Climatology, Lomonosov Moscow State University, GSP-1, Leninskie Gory, Moscow 119991, Russia

\* Correspondence: revokatova@gmail.com; gdaly.rivin@mail.ru; inna.rozinkina@mail.ru

## Motivations-Introduction

Polar lows (PLs) which are small in size and have a relatively short lifetime, can lead to a variety of extreme weather events that's why their prediction by numerical modelling is a crucial task. Appearance and development of PLs are dependent on sea ice cover, especially for the cases with a thermal nature of their formation. This study focuses on the influence of the sea ice cover in the Norwegian, Barents and Kara Seas on polar low development. Previous studies using the COSMO model focused on the various factors of polar lows formation, such as sea surface temperature, the presence and position of the ice edge, the strength and presence of a jet stream [1,2,3] and investigated the dependence of the forecast on the lead time and on the model's grid steps [4]. This work presents the first assessment of ICON model forecast of PL development in dependency on sea ice edge.

First, we have identified 7 well-developed PLs by the daily analysis of satellite images during the cold period of 2020–2021 (November–March). The area of investigation with the trajectories of the identified PLs is presented in Figure 1.

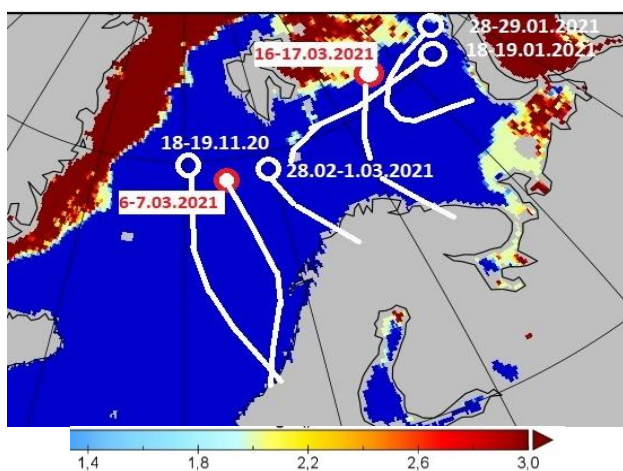


Figure 1. Trajectories of polar lows (lines) and the sea ice thickness (color). Cold period 2020–2021. The dates on the map mark the start points of the trajectories (the brown/white color of the date indicates which trajectory it belongs to). The sea ice distribution was obtained from the NSIDC (National Snow and Ice Data Center, <https://nsidc.org/home>) for 31.01.2021. The end of white lines shows the area where PL starts to break down.

The case of PL development that appeared on satellite images on January 28, 2021 in the Barents Sea is one of the most illustrative examples of the formation of PLs during the studied period. The polar low formed off the western coast of Novaya Zemlya. As can be seen from the sea ice distribution map (Fig.1) the sea was covered with ice to the east and north of Novaya Zemlya. East wind contributed to the westward transport of icy air formed over sea ice and triggered PL formation in the Barents Sea.

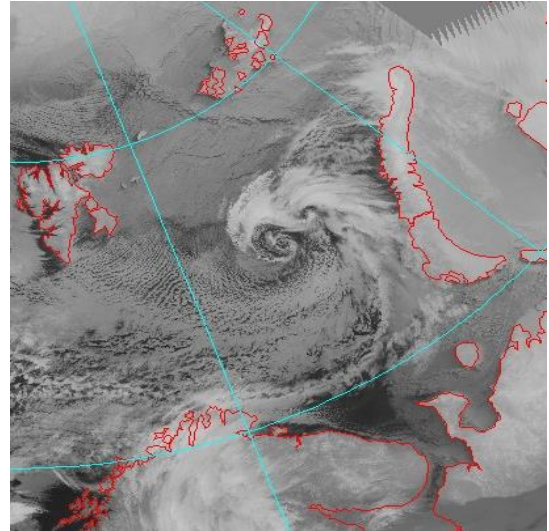


Figure 2. Satellite image of the polar low, 18:00 UTC 28.01.2021. Available from the Antarctic Meteorological Research Center (AMRC, <ftp://amrc.ssec.wisc.edu/archive>).

## Models and simulations

We used the ICON Limited-Area model [5]. The initial and boundary conditions for the ICON-LAM model in the Arctic region were taken from the global ICON model, which run at the Hydrometeorological Center of Russia in a quasi-operational mode until February 28, 2022. We have conducted three types of the model experiments: first – the control experiment without sea ice changes. Other experiments were carried out with changes in the sea ice boundary:

- 1) During a forecast, the evolution of the ice edge was specified according to the ICON analysis for the subsequent days. With this approach, changes in the position of the ice boundary during the modelled period (3 days) were small and had a very insignificant effect on the PLs forecast.
- 2) A strong artificial shift of the sea ice boundary: it was assumed that there was no sea ice south of 80N (SSIce experiment). The Kara Sea and the territory east of Svalbard were artificially freed from ice.

We have compared these two types of experiments with the control one and came to the understanding that the model sensitivity to the minimal changes in the sea ice boundary (type 1) on short (up to 3 days) time scales is insignificant. Therefore, for further assessments of the influence of the sea ice location on the formation and development of the PLs, we used more radical changes in the ice boundary - experiments of the second type (artificial shift of the boundary to the north to 80 N). It is important to note that in the SSIce experiment the ice cover is removed from the initial data, while all others meteorological parameters “remember” the existence of the

sea ice and therefore, they have the structure of the atmosphere as above sea ice (for example, inversion). This peculiarity of experiment design very likely would be reflected in the results.

We carried out numerical experiments with the ICON-Ru model in the West\_Arctic\_2km configuration, for two PL cases: 28-29.01.2021 and 18-19.11.2020. Different starting dates have been used: 02 UTC January 26, 02 UTC January 27, 02 UTC January 28. The qualitative assessment showed that the forecasts starting from 02 UTC on November 27, 2021 are most representative for our study, they more accurately reproduce the PL itself, while the model response to the modified ice field has time to form.

It follows from Fig. 3 that the absence of ice cover to the east of Novaya Zemlya (SSIce experiment) did not affect the presence of the PL and sea surface pressure (PMSL), but had an insignificant effect on the wind speed at 10 meters (V10) in the PL and the size of PL. It can be seen that by 28.01.2021 6:00 pm (40 hours lead time), the difference in wind speeds over a large area of the Arctic region reaches noticeable values. The maximum differences are achieved in the area where PL is located: the wind in the SSIce experiment slightly increases *in the center* of PL (by 4–5 m/s), while *on most part of the cloudy “comma”* the wind speed decreases (by 5-10 m/s).

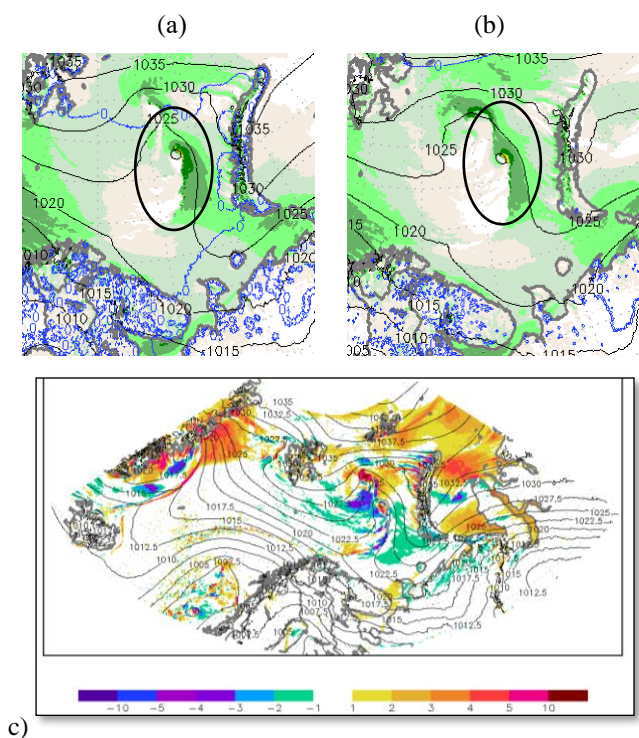


Fig. 3. Maps of PMSL and V10m for the control experiment (a) and SSIce experiment (b); difference in V10m between the SSIce and the control experiments (c). 01/28/2021, 18:00 UTC.

It should be noted how the wind speeds change over the Arctic (especially above the Kara sea), which is covered with ice in the control experiment, and is free of ice in the SSIce experiment. It is worth to notice that almost everywhere V10 increases by 1-5 m/s (Fig. 3c). This increase in V10 starts from the first hour of the forecast and periodically becomes as high as 5-10 m/s. Such changes in the wind field over a wide area are probably associated with the creation of an artificial perturbation over huge territory. This disturbance occurs due to a sharp change in the underlying surface, which is not consistent with other parameters, and it probably leads to an intensification of turbulent flows and an increase in wind speed.

Figure 4 shows the differences in PMSL between two experiments for the same date. Atmospheric pressure in the central part of the PL is lower in the control experiment, thus PL turns out to be deeper if there is “true ice” in the model. On the vast territory of the Arctic, which was artificially “liberated” from ice, there was a decrease in atmospheric pressure by 1-5 hPa.

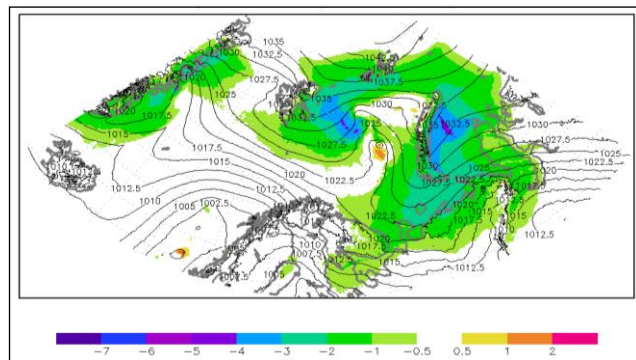


Figure 4. Differences in PMSL between the SSIce experiment and the control experiment. 01/28/2021 18:00 UTC.

### Conclusions

Our study of several cases of PL development and forecast shows that the change in the sea ice edge, even its existence is the trigger of the formation of the PL (thermal convection), does not affect the reproduction of the PL by the model. The reason for this might be the fact that initial data have prevailing influence on PL production. The meteorological fields that are used as initial data “remember” where the true ice edge is located. However, the change in the sea ice location affects the wind speed and pressure inside the PL. Changes in forecast quality related to the sea ice modification demand more deep assessment of PL development cases preferably in the areas with observational data available. We plan to continue work in this direction. Information about high-resolution simulation of polar lows during the cold season of 2019–2020 can be found in [4].

### References:

1. Nikitin, M.A.; Rivin, G.S.; Rozinkina, I.A.; Chumakov, M.M. Identification of polar cyclones above the Kara Sea waters using hydrodynamic modelling. *Vesti Gazov. Nauki* 2015, 22, 106–112. (In Russian)
2. Nikitin, M.A.; Rivin, G.S.; Rozinkina, I.A.; Chumakov, M.M. Use of COSMO-Ru forecasting system for polar low's research: Case study 25–27 March 2014. *Proc. Hydrometcentre Russ.* 2016, 361, 128–145. (In Russian)
3. Rivin, G.; Nikitin, M.; Chumakov, M.; Blinov, D.; Rozinkina, I. Numerical Weather Prediction for Arctic Region. *Geophys. Res. Abstr.* 2018, 20, EGU2018–EGU5505.
4. Revokatova, A.; Nikitin, M.; Rivin, G.; Rozinkina, I.; Nikitin, A.; Tatarinovich, E. High-Resolution Simulation of Polar Lows over Norwegian and Barents Seas Using the COSMO-CLM and ICON Models for the 2019–2020 Cold Season. *Atmosphere* 2021, MDPI, V 12, № 1, 137. <https://doi.org/atmos12020137>
5. Zängl, D. Reinert, P. Rípodas, and M. Baldauf. The ICON (ICOSahedral Non-hydrostatic) modelling framework of DWD and MPI-M: Description of the non-hydrostatic dynamical core. *Q. J. Roy. Meteor. Soc.* 2015, 141(687):563–579.

# Atmospheric River Analysis and Forecast System (AR-AFS): Sensitivity of Precipitation Forecasts in the U.S. West Coast to Microphysics and PBL Parameterizations

Keqin Wu<sup>1</sup>, Xingren Wu<sup>2</sup>, Vijay Tallapragada<sup>3</sup>, and F.M. Ralph<sup>4</sup>

<sup>1</sup>Lynker at EMC/NCEP/NOAA, College Park, MD 20740, <sup>2</sup>Axiom at EMC/NCEP/NOAA, College Park, MD 20740, <sup>3</sup>EMC/NCEP/NOAA, College Park, MD 20740, <sup>4</sup>CW3E, Scripps Institution of Oceanography, UC San Diego, CA 92093

Email: Keqin.Wu@noaa.gov

## 1. Introduction

A high-resolution regional Atmospheric River Analysis and Forecast System (AR-AFS) has been developed to provide numerical guidance for Atmospheric River (AR) forecasts and AR Reconnaissance (AR Recon). In the near real-time tests in 2022 and 2023 AR seasons, it was found that AR-AFS produced a larger negative bias in precipitation forecast than the NCEP Global Forecast System version 16 (GFSv16). Given the important role of microphysics and planetary boundary layer (PBL) processes in the numerical simulations, we examined the precipitation forecast sensitivity to the GFDL microphysical scheme, Thompson microphysics scheme, turbulent kinetic energy (TKE)-based moist hybrid eddy-diffusivity mass-flux (EDMF-TKE) PBL scheme, and Yonsei University (YSU) PBL scheme from the Common Community Physics Package (CCPP). We briefly summarize our experimental results here.

## 2. AR-AFS Model

AR-AFS is based on the FV3 dynamical core and uses initial and boundary conditions from GFSv16. The AR-AFS model has 64 vertical layers and a fine horizontal resolution of  $\sim 3$  km over the Northeast Pacific and Western North America, and provides 5 day forecasts. The physics parameterizations in the AR-AFS near real-time tests include GFS-Noah land surface, Thompson microphysics, EDMF-TKE PBL, and YSU PBL. Fig. 1 shows the model domain. It also demonstrates the capability of AR-AFS in capturing the finer structures of the observed heavy precipitation associated with an AR storm better than GFSv16, even though it predicted less precipitation than GFSv16 by about 3% over the whole domain.

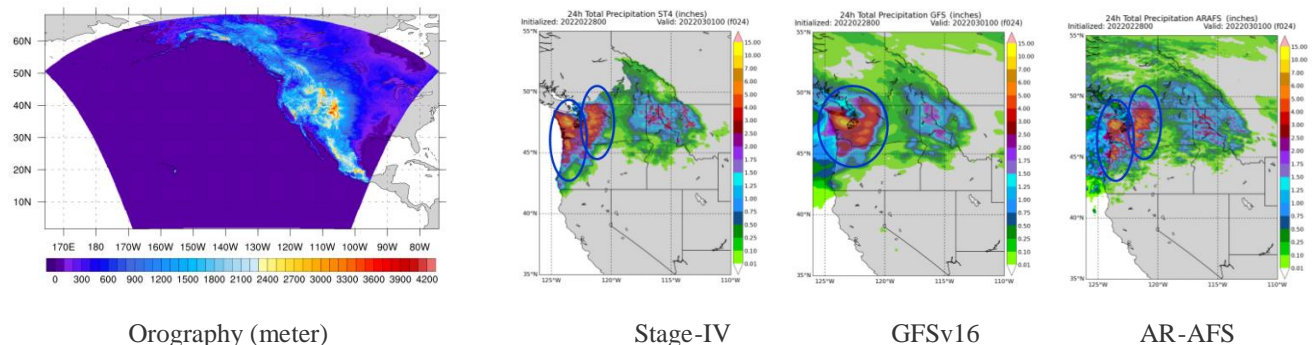


Fig. 1: AR-AFS domain (Left) and the 0-24-h accumulated precipitation ending at 00 UTC 01 March 2022 from Stage IV (ST4), GFSv16, and AR-AFS forced by the GFSv16. The Stage IV precipitation is used as the truth. The regional averages of 24-h precipitation over the regions with a cut-off of 0.1 inches in ST4 are 1.19 inches in ST4, 1.13 inches from GFSv16, and 1.09 inches from AF-AFS.

## 3. Experiments

Our experiments use a collection of atmospheric physical parameterizations under CCPP. Three CCPP suites (Table 1) are tested in our experiments, (1) *gfdlmp\_tedmf*, (2) *thompson\_gfdlsf*, and (3) *thompson\_gfdlsf\_ysu*. The comparison is made using 25 AR-AFS forecast cycles from the 2022 AR season and 15 cycles from the 2023 AR season for precipitation forecasts over the U.S. West Coast. All forecasts were initialized during the Intensive

Observation Periods (IOPs) of active ARs at 00 UTC. The hypothesis is that the Thompson microphysics scheme and YSU PBL scheme are more suitable for simulating AR associated precipitations. Fig. 2 shows the Mean Absolute Errors (MAEs) and Average Errors (biases) of precipitation forecasts from the AR-AFS, verified against Stage IV (ST4), with the three CCPP physics suites. The results are verified in the regions with a precipitation cut-off of 0.1 and 1.0 inches in ST4 over two domains in the U.S. West Coast (Fig. 2c). The MAE of *thompson\_gfdlsf\_ysu* is similar or smaller (by about 1%-7%) to that of *gfdlmp\_tedmf* and *thompson\_gfdlsf* at short lead times, but increases dramatically at long lead times. MAE of *thompson\_gfdlsf* is overall similar with that of *gfdlmp\_tedmf* and is slightly smaller than *gfdlmp\_tedmf* at all leads with the higher cut-off of 1.0 inches. Consistently high negative biases in precipitation forecast with tested physics schemes are also found (Fig.2b).

Table. 1. Overview of CCPP Suites used in the experiments with AR-AFS

Experiments/Suites	<i>gfdlmp_tedmf</i>	<i>thompson_gfdlsf</i>	<i>thompson_gfdlsf_ysu</i>
Microphysics	GFDL	Thompson	
PBL	EDMF-TKE		YSU
Surface layer	GFDL		
Land surface	GFS-Noah		
Convection	SAMF		
Radiation	GFS-RRTMG		

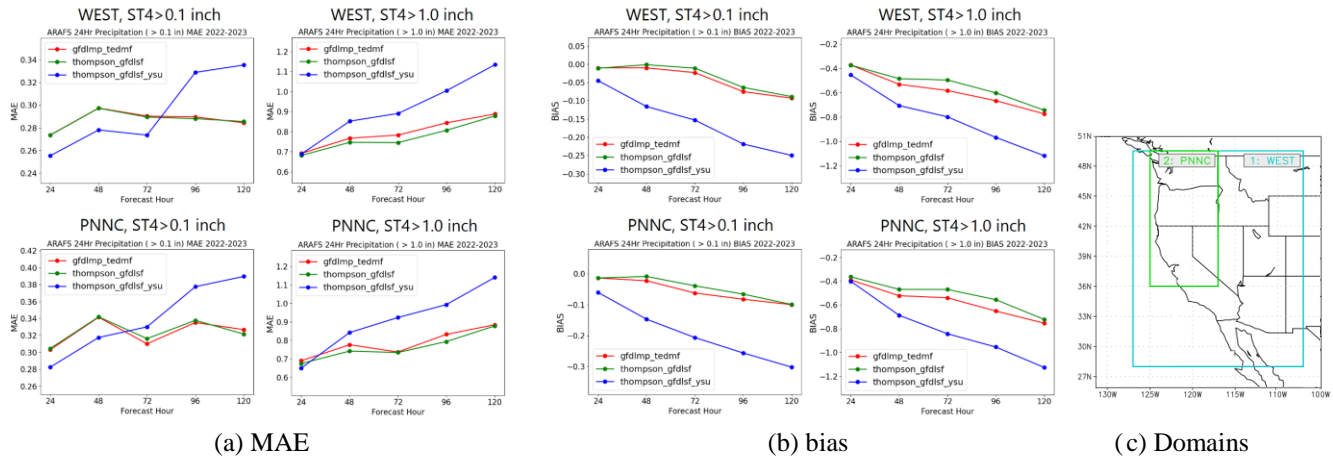


Fig. 2: AR-AFS's performance with three CCPP suites for (a) MAEs and (b) biases of the 24h precipitation forecasts with two cut-off values over two domains. (c) U.S. West Coast domain (WEST) and Pacific Northwest and Northern California regional domain (PNNC) follows Lord et al. (2023).

#### 4. Summary

For the 2022 and 2023 AR seasons, the use of Thompson microphysics scheme and GFDL surface scheme showed a potential to improve AR associated precipitation forecasts. The interesting fact that the combination of Thomson scheme and YSU scheme has lower MAEs at short leads but higher MAEs at long leads needs further investigation. The high negative biases from AR-AFS with tested physics schemes also suggest that more experiments are needed with detailed analyses.

#### Reference

Lord, S.J., X. Wu, V. Tallapragada. and F.M. Ralph, 2023. The Impact of Dropsonde Data on the Performance of the NCEP Global Forecast System during the 2020 Atmospheric Rivers Observing Campaign. Part I: Precipitation. *Weather and Forecasting*, 38, 17–45.